photonics

MDPI

Article

Continuous Domain Quasi-Bound State Enhances the Nonlinear Effects of Silicon Carbide

Ning Wang [1], Dong Pan [2], Lijing Huang [1], Liping Liu [3], Yang Liu [1], Zijie Dai [1], Xiaoxian Song [1], Zhen Yue [1,*], Jiakang Shi [4], Zhaojian Zhang [5], Kejin Wei [6], Junbo Yang [5], Jingjing Zhang [1,*] and Jianquan Yao [7]

1 Institute of Micro/Nano Optoelectronic and Terahertz Technology, Jiang Su University, Zhenjiang 210010, China
2 Beijing Academy of Quantum Information Sciences, Beijing 100193, China
3 College of Electronic Engineering, National University of Defense Technology, Hefei 230037, China
4 Nanzhi Institute of Advanced Opto-Electronic Integration, Nanjing 211800, China
5 College of Science, National University of Defense Technology, Changsha 410073, China
6 Guangxi Key Laboratory for Relativistic Astrophysics, School of Physics Science and Technology, Guangxi University, Nanning 530004, China
7 School of Precision Instruments and Opto-Electronics Engineering, Tianjin University, Tianjin 300072, China
* Correspondence: yuezhen@ujs.edu.cn (Z.Y.); 1000005146@ujs.edu.cn (J.Z.)

Abstract

We propose a silicon carbide (3C-SiC) periodic grating structure based on quasi-bound states in the continuum (q-BICs), which is used to significantly enhance the second-order optical nonlinear effect, including second-harmonic generation (SHG) and sum-frequency generation (SFG). By introducing a four-segment sub-wavelength grating on the SiC thin film and tailor the dimension, the structure successfully excites two q-BIC modes with ultra-high Q factor (resonant wavelengths at 1713.2 nm and 1804.6 nm respectively), realizing enhanced localization and nonlinear interaction of the strong light field. The simulation results show that under oblique incidence, the structure significantly enhances SFG efficiency and exhibits strong robustness to variations in key structural parameters. In addition, the study also reveals the coexistence of forward and backward SHG, and resonant wavelength tuning can be achieved by adjusting the structure dimension. This work not only provides a new path to enhance the nonlinear conversion efficiency of SiC thin films and solve the problem of difficult phase matching, but also lays the theoretical and technical foundation for the development of compact, efficient and integrated SiC-based nonlinear photonic devices.

Keywords: silicon carbide gratings; second harmonic generation; nonlinear interaction; q-BICs/quasi BIC

1. Introduction

Nonlinear optical processes [1,2], such as and SFG and double frequency conversion (SHG) [3], are one of the cores of modern photonic technology and is widely used in laser frequency conversion, quantum light source and integrated optical signal processing [4,5]. The efficiency of such processes depends on the intensity of the interaction between light and matter and the localization capacity of the light field on a sub-wavelength scale. Compared to lithium niobate and silicon, The silicon carbide (SiC), as a third-generation wide-bandgap semiconductor, exhibits unique advantages [6,7]. Silicon carbide (SiC) combines a wide transparency window (0.3–6 μm), an extremely high breakdown field (3.3 MV/cm), and excellent thermal conductivity. This allows it to withstand high-power lasers and manage heat efficiently. We selected SiC for its comprehensive advantages—broadband

Check for updates

Received: 10 February 2026
Revised: 18 March 2026
Accepted: 21 March 2026
Published: 24 March 2026

operation, high-power handling, integration potential, and stability—rather than a single record nonlinear coefficient [8–10]. In recent years, the research on SiC integrated photonics has made remarkable progress, especially towards nonlinear applications [11–18]. For example, third-harmonic generation in the visible band has been observed in the 3C-SiC nanobeam resonant cavity, and the enhanced SFG based on the SiC photonic crystal cavity. These results have preliminarily verified the potential of SiC in mid-infrared nonlinear frequency conversion and on-chip quantum light sources.

Nevertheless, the development of SiC integrated nonlinear photonic devices still faces a key bottleneck: Although SiC itself is non-centrosymmetric (point group 43 m) and exhibits bulk second-order nonlinearity, achieving efficient second-order processes in conventional SiC waveguides remains challenging due to strict phase-matching requirements and limited mode overlap [19]. However, in metasurfaces, the introduction of specific geometric asymmetries (symmetry defects) allows for the artificial induction of strong effective second-order nonlinear polarisation at the local level, thereby circumventing the reliance on conventional phase matching and directly realising efficient second-order nonlinear optical effects at the ultrathin scale [20]. In particular, Radulaski et al. demonstrated the feasibility of 3C-SiC microcavities for frequency conversion, paving the way for the development of highly efficient on-chip nonlinear light sources [21]. Meanwhile, Shi et al. introduced strong structural asymmetry by etching waveguides at the sidewalls and the top-sidewall junctions. This interfacial effect breaks the overall symmetry, thereby activating the intrinsic second-order nonlinear susceptibility of silicon carbide [22]. These results preliminarily demonstrate the potential of SiC metasurfaces for applications such as mid-infrared nonlinear frequency conversion and on-chip quantum light sources.

In these studies, the level of the Q factor has become a crucial factor. q-BICs are realized in the open structure through symmetry breaking, transforming theoretically resonant states with infinite Q factor into practically applicable high-Q resonances, which simultaneously maintain free-space radiation coupling and enable strong light field localization and enhanced light–matter interaction [23–26]. In addition, traditional optical fiber communication C-band (1530–1565 nm) and L-band (1565–1625 nm) resources are becoming increasingly scarce, while 1700–1800 nm is an exploratory region for extending to longer wavelengths and can be used to increase communication capacity.

To this end, this study proposes and demonstrates an innovative scheme based on periodic grating q-BICs to address the bottleneck in SiC nonlinear conversion efficiency. By designing a subwavelength grating structure of SiC and performing structural optimization, a q-BIC resonance mode with strong localization of the light field within the nonlinear material is achieved. This structure enables sum-frequency conversion efficiency at the 10^{-2} level. By adjusting the structural parameters, resonant wavelength tuning and control can be achieved. At the same time, benefiting from the nanoscale compactness, the structure offers the advantages of being ultra-compact and monolithically integrable.

2. Symmetry-Broken Dual Quasi-q-BIC

Within the theoretical framework of bound-in-continuum states (BIC), the electromagnetic response of a system can be described by a non-Hermitian Hamiltonian model [27]. For a two-mode coupled system, its Hamiltonian can be expressed as:

$$H = \begin{pmatrix} \omega & k \\ k & \omega \end{pmatrix} - i \begin{pmatrix} \gamma & \gamma e^{i\varphi} \\ \gamma e^{i\varphi} & \gamma \end{pmatrix} \tag{1}$$

In this context, ω represents the natural frequency of the mode, k denotes the inter-mode coupling strength, γ signifies the radiation loss, and φ indicates the phase factor. The intrinsic frequency of this system is:

$$\omega_{\pm} = \omega \pm k - i\gamma(1 \pm e^{i\varphi}) \tag{2}$$

Under ideal symmetry conditions where $\varphi = 0$, the system supports perfect BIC modes with zero imaginary parts of their eigenvalues, corresponding to infinite quality factors (Q factor). When symmetry breaking is introduced (e.g., through the geometric parameter α), the system Hamiltonian expands to a more general form:

$$H = \begin{pmatrix} \omega_A & k \\ k & \omega_B \end{pmatrix} - i \begin{pmatrix} \gamma_1 & \sqrt{\gamma_A \gamma_B} \\ \sqrt{\gamma_A \gamma_B} & \gamma_B \end{pmatrix} \tag{3}$$

The corresponding natural frequency is:

$$\omega_{\pm} = \frac{(\omega_A + \omega_B) - i(\gamma_A + \gamma_B) \pm \sqrt{[(\omega_A - \omega_B) - i(\gamma_A - \gamma_B)]^2 + 4(k - i\sqrt{\gamma_A \gamma_B})^2}}{2} \tag{4}$$

This expression clearly reflects the impact of symmetry breaking on the mode frequency and loss. When the following critical condition is satisfied:

$$k(\gamma_A - \gamma_B) = \sqrt{\gamma_A \gamma_B}(\omega_A - \omega_B) \tag{5}$$

This condition represents a balance between the coupling strength k and the asymmetry-induced differences in mode frequencies and radiation losses. Physically, it describes the point at which the two resonant modes become maximally hybridized while maintaining minimal net radiation loss, thereby enabling the formation of dual high-Q quasi-BIC resonances. In our design, the asymmetry parameter $\alpha = \frac{\Delta d}{D_0}$ directly influences this balance. As α increases, the widths of the two air gaps (Db and Dc) become increasingly unequal, breaking the mirror symmetry of the unit cell. This leads to a gradual detuning of the mode frequencies ($\omega_A \neq \omega_B$) and a redistribution of radiation losses ($\gamma_A \neq \gamma_B$), while the coupling strength k remains largely governed by the periodic modulation. When the structural parameters are tuned such that Equation (5) is approximately satisfied, the system enters a regime where both quasi-BIC modes exhibit simultaneously high Q factors and strong field confinement. The four-segment grating structure designed in this paper realizes a dual-quasi BIC mode by adjusting α, and its resonant behavior can be precisely described by the aforementioned theoretical model.

The structure is based on the silicon carbide platform design on the insulator, and is composed of the SIC layer deposited on the substrate and its four-segment periodic grating at its top. In order to ensure the effective transmission of the guide mode, the equivalent refractive index of the grating and the substrate material should be lower than that of the SIC layer. SiO_2 has become a medium widely used in silicon carbide platforms in linear and nonlinear optical applications, so we choose it as the material for gratings and substrates. Figure 1 shows a schematic of the unit cell of the structure as well as the diagram of sum-frequency and second-harmonic generation. The period of the cell of the unit is P = 800 nm, the thickness of the SIC layer is $H_{\mathrm{SiC}} = 330\,\mathrm{nm}$, the substrate is assumed to be semi-infinite, and the grating unit consists of four parts: the first and third parts of the materials are SiO_2, with the same width $D_a = 0.15P$ and the same trapezoidal slope θT, the same height $H_{\mathrm{SiO_2}} = 300\,\mathrm{nm}$, the second and fourth parts are air gaps, and the widths are set to $D_b = D_0 - \Delta d$ and $D_c = D_0 + \Delta d$ respectively, where $D_0 = 0.35P$ is the initial width. By introducing the geometric parameter $\alpha = \frac{\Delta d}{D_0}$ $(0 < \alpha < 1)$, the width difference between the air gaps is regulated, thereby introducing a controllable asymmetric perturbation into the structure. This perturbation promotes the transformation of the original ideal bound state (BIC) into a quasi-BIC mode, and then excite two guide mode resonances with ultra-high-quality factors (Q factor) in the grating. This resonance mechanism effectively localizes the electric field and provides the field enhancement necessary for nonlinear optical processes.

Sum-frequency generation (SFG) refers to the process in which two photons of different frequencies interact and "merging" in nonlinear crystals to produce a new photon with a higher frequency (more energy) [28,29]. Two input photons (frequency ω_1 and ω_2 respectively) are absorbed by the medium, and an output photon (frequency ω_3) is generated at the same time. This process follows the law of conservation of energy, that is, $\omega_3 = \omega_1 + \omega_2$. This means that the frequency of the output light is the sum of the two input light frequencies. In order to realise efficient conversion, it is also necessary to satisfy momentum conservation, that is, $k_1 + k_2 = k_3$ (where k is the wave arrow). This condition is known as phase matching in nonlinear optics. In addition, SHG is a special case of SFG in which the two input photons have identical frequencies. Two exactly the same photons (both frequencies are ω_1) combined in a nonlinear crystal to produce a new photon with a double frequency, that is, $\omega_3 = 2\omega_1$. Therefore, SHG is also commonly referred to as "second-harmonic generation".

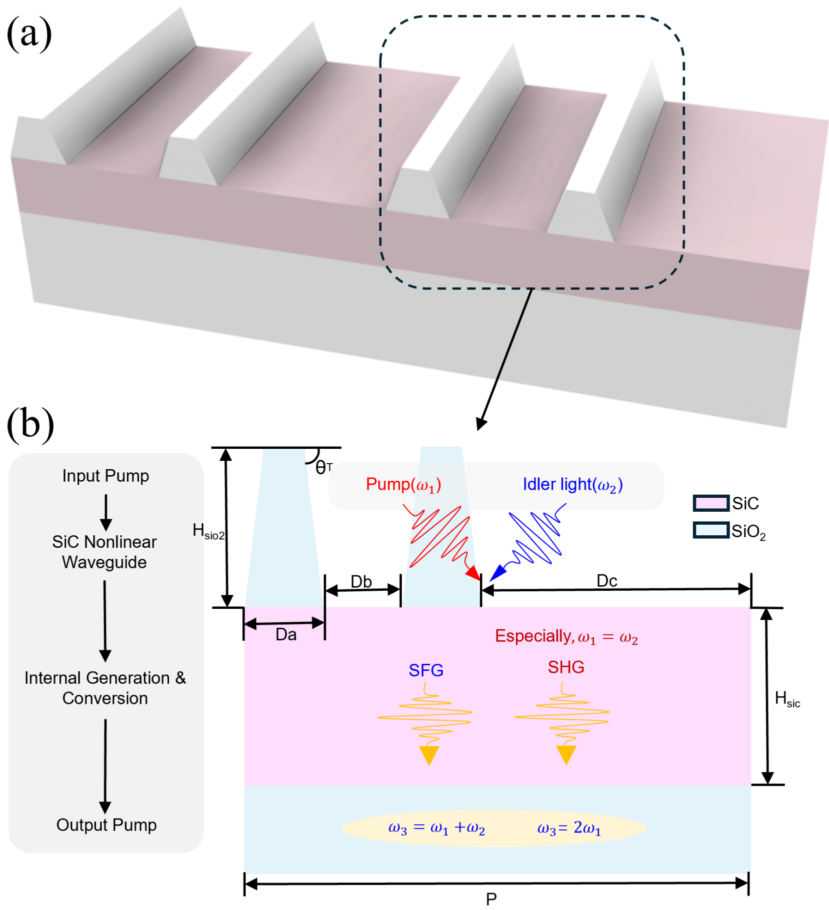

Figure 1. (**a**) Schematic diagram of the periodic grating structure. (**b**) Cross-sectional view of the unit cell and the energy diagram of the SFG process.

We use COMSOL Multiphysics 6.3 for simulation modeling: periodic boundary conditions are set in the x direction, and a perfectly matched layer is set in the y direction. The transverse electric (TE) polarised plane wave (the electric field is parallel to the z-axis) is incident at an oblique angle θ. The refractive index data of SiC comes from the experimental measurement value, and its maximum second-order nonlinear tensor component d_{33} is arranged in parallel with the incident polarisation. Figure 2a,b show the change law of $\theta = 4°$ and BIC. In the ideal structure, energy is perfectly bound in the structure and cannot be leaked into free space through any radiation channel. It is because they are not coupled with the outside world that the plane waves emitted from the outside cannot directly excite these "True BIC". When we introduce an asymmetry parameter into the structure, it breaks the original symmetry. We change the parameter α. When $\alpha \neq 0$, the unit cell no longer possesses perfect mirror symmetry. This symmetry breaking opens a radiation channel for the BIC, transforming the originally perfect, infinitely high-Q BIC into a quasi-BIC that can couple to free-space radiation. At this time, the Q factor changes from infinity to a finite but still very high value. Through the external incident light, the quasi-BIC mode can be excited, which is manifested as a sharp resonance valley in the transmission spectrum.

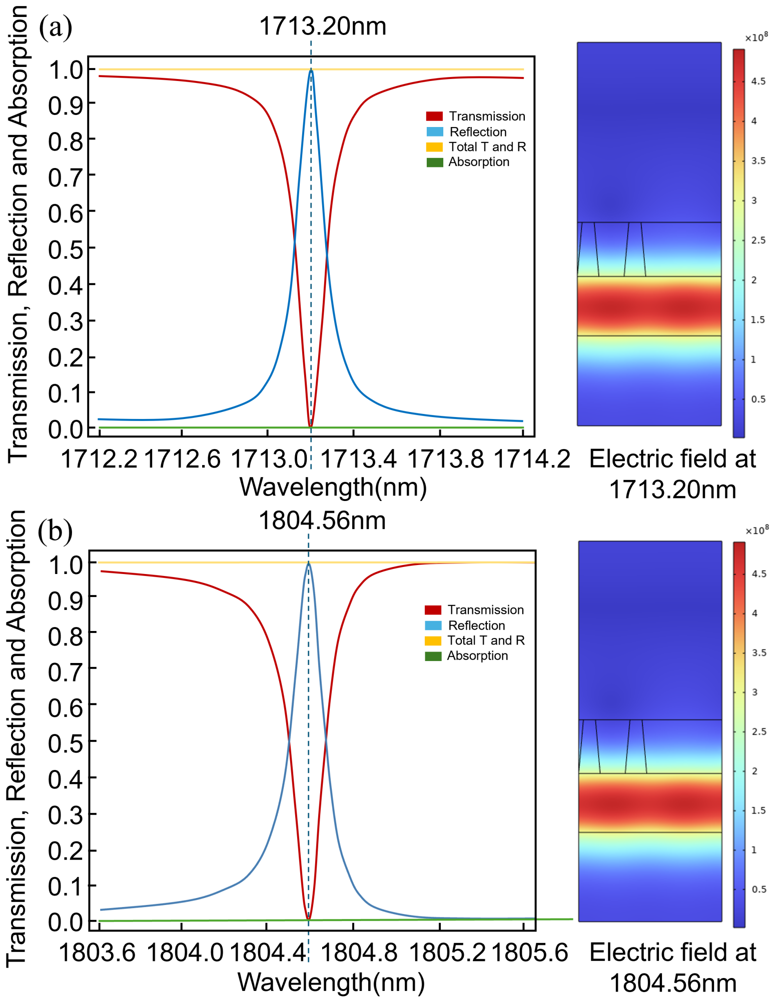

Figure 2. (**a**) Resonant dip near 1712.2 nm (q-BIC1) and the electric field intensity diagram. (**b**) Resonant dip near 1804.6 nm (q-BIC1) and the electric field intensity diagram.

The key to realizing the "double-peak" quasi-BIC lies in Brillouin zone folding. In a symmetrical grating with a period of P, its energy band structure (the relationship between electromagnetic mode frequency and wavevector) exists within a region known as the Brillouin zone. As illustrated below, Figure 3a presents the band structure diagram for the period $P' = P/2$, while Figure 3b presents the band structure diagram for the period P. When a perturbation with period P is applied to a grating with a fundamental period of

$P' = P/2$, an equivalent superlattice structure with doubled period ($P = 2P'$) is formed. At this point, the new wave vector becomes $G_{\text{new}} = 2\pi/P = 0.5G_{\text{old}}$. Modes originally situated at the boundary of the old Brillouin zone ($k = \pi/P$), whose wave vectors are precisely integer multiples of Gnew, are consequently 'folded' back into the new Brillouin zone. The progression from Figure (a) to (b) clearly demonstrates that introducing a periodic perturbation folds modes originally within the light cone to its exterior. Two guided modes, previously situated at distinct positions in momentum space, now appear near the same momentum point after folding and become degenerate. At this point, introducing the asymmetry parameter α simultaneously breaks the symmetry of these two folded modes, transforming them both into quasi-BICs. This manifests in the transmission spectrum as two independent high-Q resonance valleys (q-BIC1 and q-BIC2).

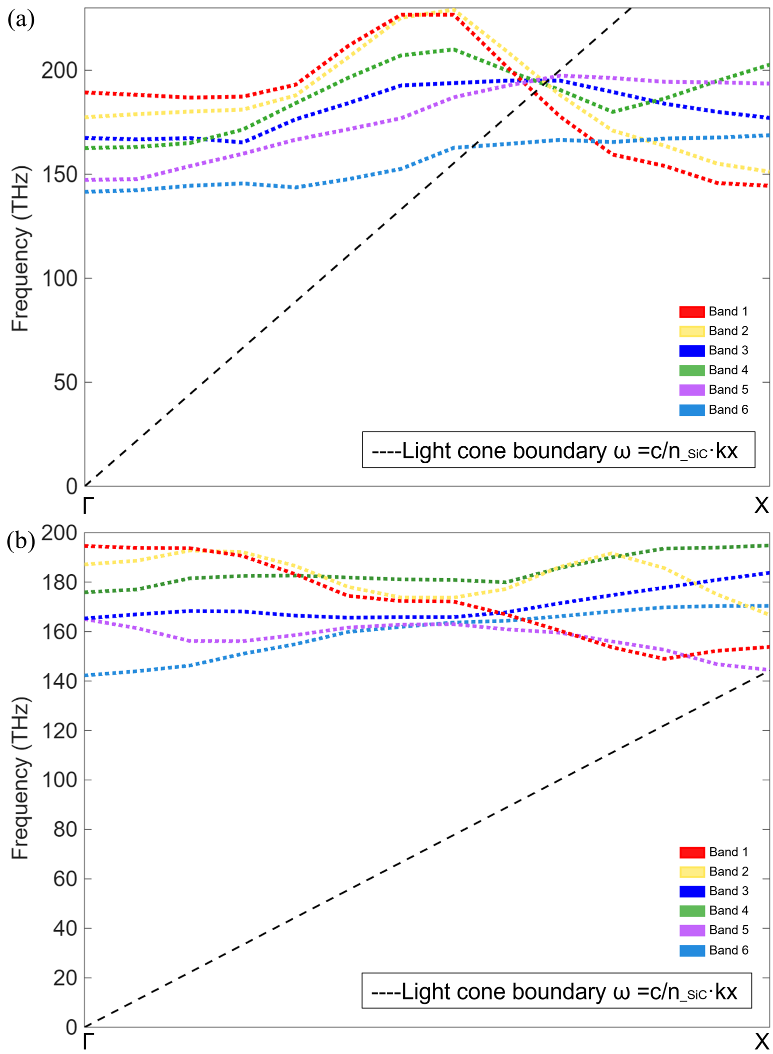

Figure 3. (**a**) Band structure diagram at a period of 0.5P. (**b**) Band structure diagram for a period of P.

In order to obtain better light field confinement, we have optimized the structure on the basis of the traditional rectangular grating. In the optical resonant cavity, the Q factor is defined as $Q = \omega \times (\text{stored energy}/\text{energy lost per second})$. The higher the Q factor, the longer the energy is stored in the cavity, the sharper the resonance peak, and the lower the loss, so the loss is the determining factor of the Q factor [30,31]. The side wall of the trapezoidal grating is inclined. The inclined side wall means that the transition from the grating core (high refractive index) to the cladding (low refractive index) is not mutant, but a gradient area, which makes the distribution of the light field smoother and more gentle. Because the refractive index is gradual, the peak of the light field distribution tends to shift toward the upper center of the grating. So the main energy part of the light field is "pushed" away from the rough physical sidewall; at the same time, the overlap integral between the light field and the sidewall roughness is greatly reduced, and the scattering loss induced by the roughness is significantly suppressed. As shown in Figure 4a, we explored the relationship between the slope angle of the side wall of the trapezoidal structure and the Q factor. The taper angle design integrates theoretical optimization with practical manufacturing process compatibility. In 2024, Rahmouni et al. detailed the fabrication process for micro-ring resonators on 4H-SiC platforms on insulators, covering critical steps such as dry etching. The trapezoidal taper angle design proposed in the paper was experimentally validated for feasibility, and the process methodology demonstrated the feasibility of achieving specific taper structures through controlled etching [32]. In order to avoid the trapezoidal grating from becoming a triangle, we chose a tilt angle of 80° to 90°. It can be seen from the figure that as the tilt angle increases, the Q factor decreases. In order to consider the difficulty of process manufacturing and the impact of side wall inclination at the same time, we have selected 85° for the side wall inclination angle in our structure, and the Q factor at the resonance wavelength are 11,850 (1713.2 nm) and 10,809 (1804.6 nm) respectively.

Due to the constant filling ratio of SiO_2 [33], the resonance wavelength here is quite stable relative to the increase of α. As shown in Figure 4b, the position of the resonance wavelength hardly changes with the increase of α.

At the same time, we verified the robustness of the structure. Figure 4c shows the resonance wavelength shift as the single-sided grating width deviates from the design value β. Surprisingly, even within the range of $\pm 25\%$ of β change, the position of the resonance wavelength only fluctuates slightly. This phenomenon is attributed to the physical nature of the q-BIC mode: its high Q factor and strong field localization ability come from the symmetry breaking mechanism itself, not the extremely sensitive dependence on geometric parameters. As long as the symmetry gap exists, the quasi-BIC mode can be excited and can maintain excellent light field confinement.. This robustness greatly reduces the process difficulty in nanoprocessing and improves the consistency and reliability of the device.

In addition to the grating geometric parameter α, the incident angle θ of the plane wave is also an important factor in breaking the structural symmetry and in the excitation and tuning of the quasi-BIC modes. Figure 4d clearly shows the evolution law of the transmission spectrum with the change of the incident angle θ when the fixed grating geometric disturbance $\alpha = 0.5$. It can be observed that with the gradual increase of the incident angle θ, the double quasi-BIC mode (q-BIC1 and q-BIC2) that originally existed at a specific angle showed a significant separation trend, and the corresponding resonance peaks move further apart along the wavelength axis.

This separation phenomenon stems from the additional tangential wavevector component ($k\_x = (\omega/c) \times \sin\theta$) introduced by the change of the angle of incidence. This component directly participates in the phase matching conditions of guided-mode resonance. For two quasi-BIC modes with different equinom wave arrows, the wavelength required for resonance will be shifted at different rates with the change of θ, resulting in an increase in the resonance peak spacing. It is especially important that although the resonance wavelength changes drastically with θ, at every specific incident angle, once excited, the quasi-BIC still exhibits strong field localization at its resonance wavelength. This shows that even under a large θ, the symmetry break introduced by the incident angle mainly affects the excitation conditions (resonance position) of the pattern, rather than significantly degrading its intrinsic field enhancement capability. Therefore, near the resonance wavelength, the electromagnetic field energy is still efficiently bound in the SIC layer, maintaining a very high energy density, which is crucial for using angle tuning to achieve efficient nonlinear frequency conversion.

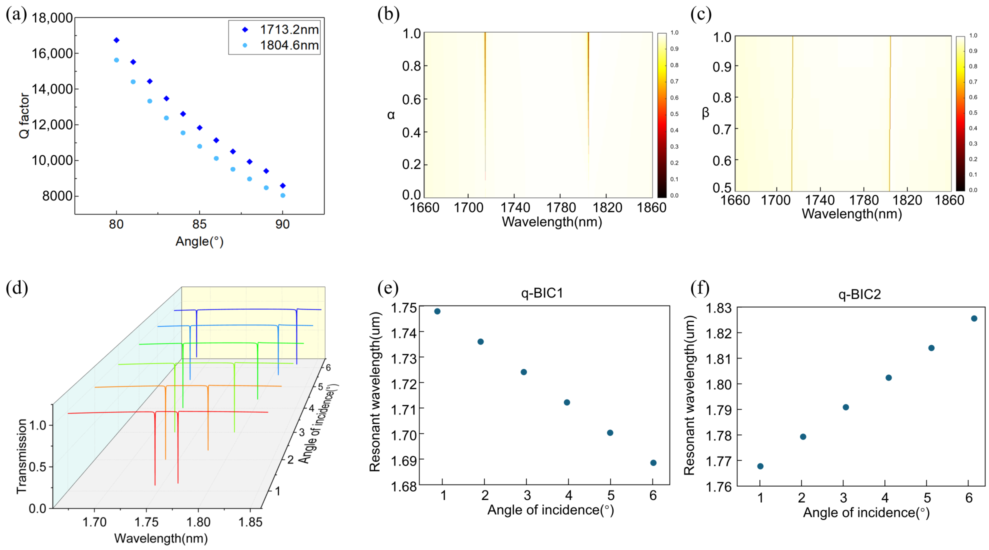

Figure 4. (**a**) Relationship between the Q-factor and the trapezoidal slope function in the SIC layer. (**b**) Transmission spectrum of the grating structure as a function of the grating geometry parameter α when the incident angle is 4°. (**c**) Transmission spectrum as a function of the single-sided grating structure parameter β when the incident angle is 4° and the structure parameter α = 0.5. (**d**) Transmission spectrum variation with incident angle at structural parameter α = 0.5. (**e**) Position shift of the resonance peak at q-BIC1 with changing incident angle. (**f**) Position shift of the resonance peak at q-BIC2 with changing incident angle.

Further investigations reveal that as the incident angle θ gradually increases from 1° to 6°, the wavelength shifts corresponding to the resonance peaks of the two quasi-BIC modes (q-BIC1 and q-BIC2) are quantifiable. As shown in Figures 4e,f, this angle-dependent resonance exhibits clear reversibility and monotonicity, enabling the actual angle of incidence to be back-calculated by precisely measuring the resonance peak position. Therefore, this structure not only serves as an efficient nonlinear frequency conversion element but also finds application in integrated optical sensing and angle detection. It enables optical readout functionality that "directly quantifies the incident angle through resonance peak position," providing a novel technical pathway for developing multifunctional, high-sensitivity on-chip photonic devices.

3. Second-Order Nonlinear Processes in Silicon Carbide Resonant Gratings

Based on the strong field localization characteristics supported by the above-mentioned dual quasi-BIC, we further study the SHG and SFG processes in the design structure (SHG being a special case of SFG when $\omega_1 = \omega_2$). A three-step coupled-wave model (including the non-depleted pump approximation) is employed for accurate calculation.

First, pump wavelength simulation: under the fixed angle of incidence $\theta = 4°$ and the grating parameter $\alpha = 0.5$, solve the electromagnetic field distribution at the pump wavelength λ (corresponding to the quasi-BIC resonance wavelength); calculate the second-order nonlinear polarisation intensity $P(2\omega)$ induced in the SiC layer based on the field distribution; finally, $P(2\omega)$ As the source term, solve the radiation field at the harmonic wavelength λ, and the SHG power is obtained by integrating the Poynting vector over the output plane on the substrate side.

3C-SiC belongs to the cubic crystal system with 43 m point group symmetry, and its effective second-order nonlinear tensor has only one independent component d_{36}. When the pump light is polarised along the crystal direction of SiC (corresponding to the maximum $d_{36} \approx 16.6$ pm/V), nonlinear polarisation can be expressed as:

$$P_z(2\omega) = 4\epsilon_0 d_{36} E_x E_y \tag{6}$$

The pump field components need to be aligned with the crystal axis to maximize nonlinear coupling. In the simulation, TE polarization (electric field along the z-axis) is set to match the d_{36} optimized direction of SiC, with the pump intensity fixed at 100 MW/cm^2.

In the process of doubling frequency, we found an interesting phenomenon. The propagation direction of the newly generated double-frequency light ($\omega 3$) has two directions of the same and opposite directions relative to the pumped light, which is defined as "forward SHG" and "backward SHG". Forward SHG is typically generated under conventional phase-matching conditions. However, the conditions for the appearance of backward SHG are relatively stringent. Unlike its forward counterpart, which satisfies the conventional phase-matching condition $k3 = k1 + k2$, backward SHG arises from the momentum compensation provided by a periodic structure. It satisfies the reverse phase-matching condition: $k3 = k1 + k2 - \mathrm{G}$, where G = $2\pi/\Lambda$ is the reciprocal lattice vector provided by the periodic structure with period Λ. This condition dictates that the wavevector of the generated sum-frequency light (k3) is opposite in direction to that of the pump light (k1 and k2), leading to the distinctive backward-propagating signal [34–36]. It can be seen from Figure 5a,b that the forward SHG conversion efficiency at 1713.2 nm can reach 2.33×10^{-3}, the backward SHG conversion efficiency can reach 3.95×10^{-5}, and the forward SHG conversion efficiency at 1804.6 nm can reach 1.17×10^{-4}, the backward SHG conversion efficiency is 1.40×10^{-5}. Forward SHG has become a cornerstone of nonlinear optics, supporting a vast range of applications and technologies, while backward SHG holds great promise in fields such as unidirectional lasers and quantum information science [17,37].

With the support of the aforementioned dual quasi-BIC resonance mode, we further studied the broader second-order nonlinear process—and SFG—in this structure. In the SFG process, two beams of pump light with different frequencies (ω_1, ω_2) interact within the nonlinear medium to produce sum-frequency light with a frequency of $\omega_3 = \omega_1 + \omega_2$. The conversion efficiency of this process strongly depends on the phase-matching condition and the local electric field intensity.

We adopt a three-step coupled-wave model consistent with SHG analysis. Under the non-depleted pump approximation, we solve the electric field distribution of two beams of pump light (λ_1, λ_2) in the structure respectively, calculate the induced nonlinear polarisation intensity $P^{(2)}(\omega_3)$, and then solve for the radiated sum-frequency power. The normalized conversion efficiency of SFG can be expressed as:

$$\eta_{SFG} = \frac{P_{out}(\omega_3)}{P_{in}(\omega_1)P_{in}(\omega_2)} \propto |\chi^{(2)}_{eff}|^2 \cdot Q_1 Q_2 Q_3 \cdot V^{-1}_{eff} \tag{7}$$

Among them, Q1, Q2 and Q3 are the quality factors of the two pumping modes and the frequency mode respectively, V^{-1}_{eff} is the effective mode volume, and $\chi^{(2)}_{eff}$ is the effective second-order nonlinear coefficient. Our system scanned the pump wavelength pair (λ_1,λ_2), and fixed the angle of incidence $\theta = 4^\circ$, and the grating parameter $\alpha = 0.5$. Figure 6a,b show the two-dimensional mapping of the change of SFG efficiency with λ_1 and λ_2. It can be clearly observed that when any pump wavelength is close to the quasi-BIC resonance wavelength (1713.2 nm and 1804.6 nm), the conversion efficiency is significantly improved, forming an obvious efficiency "ridge line". Especially when the two pumps resonate at the same time (i.e. λ_1, λ_2 match q-BIC1 and q-BIC2 respectively), the frequency conversion efficiency reaches 2.99%, which is more than four orders of magnitude higher than that of non-resonance. This result fully confirms the synergistic enhancement effect of the dual quasi-BIC modes on the SFG process.

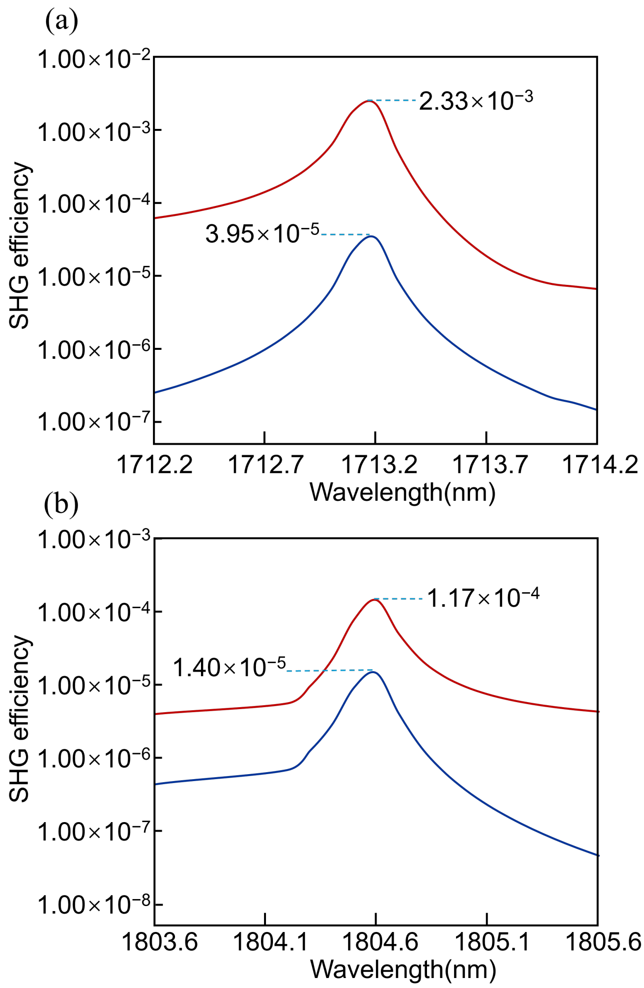

Figure 5. (**a**) Second-harmonic conversion efficiency as a function of the incident wavelength (At the resonance wavelength of 1713.2 nm). (**b**) Second-harmonic conversion efficiency as a function of the incident wavelength (At the resonance wavelength of 1804.6 nm).

In order to further evaluate the practicality and tunability of the structure, we focused on the sensitivity of SFG efficiency to changes in the width of the grating. With the structural parameter $\alpha = 0.5$ and the angle of incidence $\theta = 4°$ kept fixed, we changed the width of the grating and calculated the corresponding SFG efficiency.

Figure 7a,b show the SFG efficiency as a function of grating width (0.11P–0.19P). It can be observed that with the increase of the grating width, the wavelength corresponding to the peak conversion efficiency redshifts. The core reason is the inverse relationship between "phase mismatch tolerance" and "spectral bandwidth". For the generation of and frequency, it is assumed that the pump light frequency is $\omega 1$, the signal light frequency is $\omega 2$, and the light frequency of the and frequency is $\omega 3 = \omega 1 + \omega 2$. The perfect quasi-phase matching condition is: $\Delta k = k_F - k_p - k_s - 2\pi/\Lambda = 0$. When this condition is met, all light waves involved in nonlinear interactions always maintain phase coherence during propagation, and the frequency light is continuously and coherently enhanced, and the conversion efficiency is the highest.

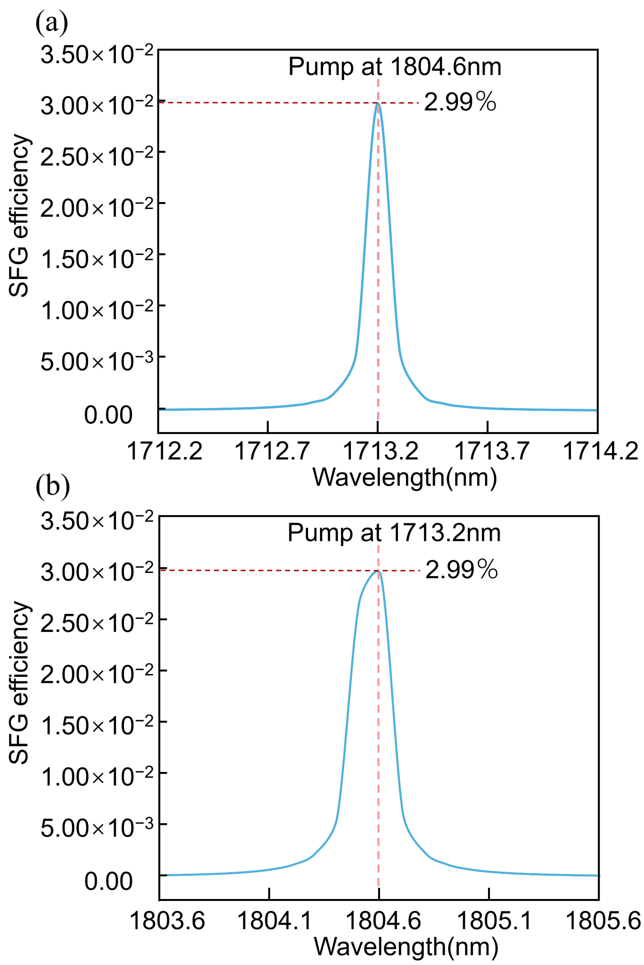

Figure 6. (**a**) Sum-frequency conversion efficiency as a function of the incident wavelength (At the resonance wavelength of 1713.2 nm). (**b**) Sum-frequency conversion efficiency as a function of the incident wavelength (At the resonance wavelength of 1804.6 nm).

In the actual system, due to small changes in wavelength, temperature or angle, phase mismatch $\Delta k \neq 0$ will occur. The nonlinear conversion efficiency η is proportional to the square of the interaction length Da (i.e., the grating width), but at the same time, it is modulated by a sinc^2 function: $\eta \propto L^2 \times \mathrm{sinc}^2(\Delta k \times L/2)$. This sinc^2 function takes the maximum value of 1 when $\Delta k = 0$, when $|\Delta k \times L/2|$ When $=\pi$, it drops to zero for the first time. The width of the sinc^2 function (that is, tolerance range for phase matching) is inversely proportional to the interaction length Da. When the grating is shorter: the sinc^2 function is a "fat" peak, which means that even if Δk deviates more from 0 (that is, the wavelength deviates more from the ideal value), it can still maintain a high conversion efficiency. Therefore, the short gratings possess a broad phase-matching spectral bandwidth; the peak efficiency spans a wider wavelength range and is less sensitive to exact phase matching. When the grating is long: the sinc^2 function becomes a "tall and narrow" peak. It is extremely sensitive to phase mismatch Δk. As long as Δk has a slight deviation, the efficiency will drop sharply. Therefore, long gratings exhibit a narrow phase-matching bandwidth.

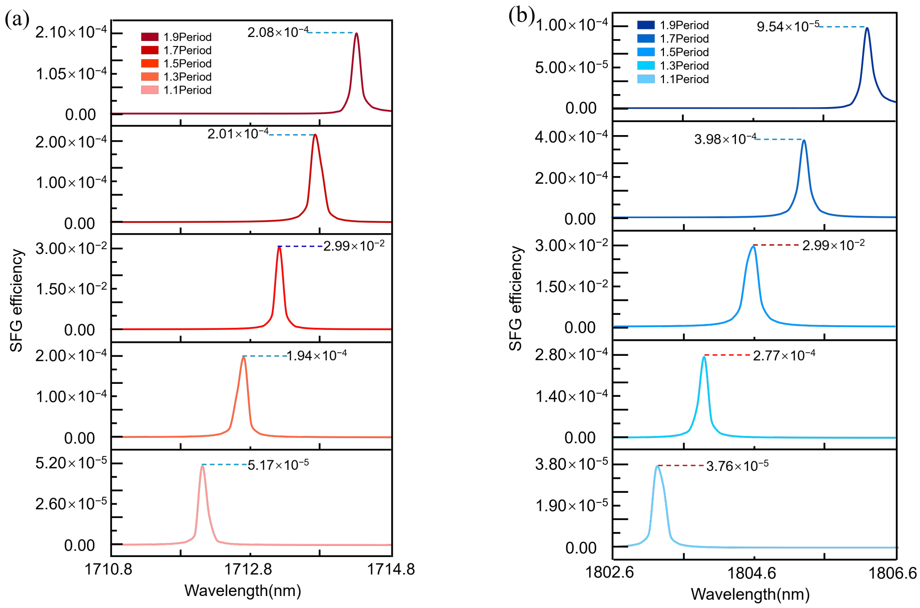

Figure 7. (**a**) Near 1712.8 nm, the sum-frequency conversion efficiency changes with the variation of the dual grating width, showing a redshift phenomenon. (**b**) Near 1804.6 nm, the sum-frequency conversion efficiency changes with the variation of the dual grating width, showing a redshift phenomenon.

The observed "redshift" of the SFG efficiency peak with increasing grating width can be attributed to the combined effect of phase-matching bandwidth and material dispersion. The conversion efficiency is governed by a sinc^2 $(\Delta k \times L/2)$ function. For a longer grating (larger L), the spectral width of this function narrows, making the process highly sensitive to phase mismatch ($\Delta k \neq 0$). In a real system, small, unavoidable background phase mismatches (δ) exist due to fabrication tolerances. To achieve maximum efficiency with a long grating, the wavelength must be slightly detuned to introduce an opposing Δk that compensates for δ (i.e., $\Delta k \times L/2 + \delta \approx 0$). Given the normal dispersion of the material in this spectral range (refractive index decreases as wavelength increases [36,38]), compensating for a typical positive background mismatch requires shifting the wavelength to a longer value. This results in the observed redshift of the peak efficiency wavelength.

4. Discussion

In terms of nonlinear conversion efficiency, the 2.99% SFG efficiency and SHG efficiency on the order of 10^{-3} achieved in this work demonstrate significant competitiveness among similar all-dielectric metasurfaces based on q-BICs. Regarding SFG, recent studies on AlGaAs dielectric metasurfaces have shown that the SFG process can be enhanced in the 500–600 nm visible light band through the synergistic excitation of multiple quasi-BIC resonances; however, these studies did not explicitly report specific conversion efficiency values [39]. In contrast, this work achieves a conversion efficiency of nearly 3% in the communication band via dual-wavelength pumping, clearly demonstrating the advantages of synergistic enhancement through dual BIC resonances. Regarding SHG, compared with other types of all-dielectric platforms—such as GaAs-based dielectric resonator metasurfaces with an efficiency of 2×10^{-5} [40], $LiNbO_3$ guided-mode resonator metasurfaces with an efficiency of 0.136% [41], and $LiTaO_3$ guided-mode resonator metasurfaces with an efficiency of 0.042% [42]—where SHG efficiencies typically hover between 10^{-5} and 10^{-3}, This work simultaneously achieves forward and backward harmonic generation in the SiC material system and elevates the SHG efficiency to 0.233% under dual-resonance conditions. These advantages are attributable to the excellent comprehensive optical properties of SiC and the ingenious design of the symmetry-breaking structure.

5. Conclusions

Through theoretical design and numerical simulation, this research has successfully constructed and verified a silicon carbide grating structure based on a quasi-bound state in the continuum (q-BIC), and achieved remarkable results in improving the efficiency of second-order nonlinear optical conversion. Specifically, when the structure introduces a symmetry-breaking parameter α = 0.5 and the angle of incidence θ = 4°, the structure excited two quasi-BIC modes at 1713.2 nm and 1804.6 nm respectively, and their Q factor reach 11,850 and 10,809 respectively. Under this resonance condition, the efficiency of SHG is up to 2.33×10^{-3}, and forward and backward harmonics are observed simultaneously; under dual-pump collaborative resonance, the efficiency of SFG is improved by more than four orders of magnitude compared with non-resonance, reaching 2.99%. The structure still maintains stable performance within the range of ±25% of grating width variation, showing good process tolerance and wavelength tuning ability. These results fully demonstrate that the q-BIC-SiC structure has significant advantages in realizing high-efficiency nonlinear frequency conversion.

Based on the aforementioned performance characteristics, this structure holds clear application prospects in the future field of highly integrated photonic chips. These include serving as an on-chip wavelength converter for optical communications, generating quantum light sources based on inverse harmonics, and enabling tunable harmonic generation for nonlinear signal processing. Concurrently, we observe that integrating two-dimensional materials enhances second-order nonlinear efficiency. For instance: in silicon waveguides coated with $MoSe_2$, the second harmonic generation (SHG) signal intensity increases approximately fivefold; in optical fibres coated with WS_2, SHG intensity grows by about twentyfold; whilst integrating WSe_2 into photonic crystal microcavities boosts SHG conversion efficiency by over two hundredfold [43]. Subsequent research will focus on the experimental fabrication of this structure, concentrating on: dry etching processes for integrating two-dimensional materials and nanoscale gratings onto silicon carbide insulators, which may face critical challenges such as material loss and interfacial defects, including etching-induced surface damage and issues at the SiC/SiO_2 interface; and the systematic characterisation of nonlinear conversion efficiency and spectral response under actual excitation conditions. This will facilitate the transition from theoretical modelling to practical device design.

Author Contributions: Conceptualization, D.P. and L.L.; Methodology, D.P., Z.D., K.W. and J.Y. (Jianquan Yao); Software, N.W., Z.Y. and J.Y. (Jianquan Yao); Validation, L.H., Z.Z. and J.Y. (Junbo Yang); Formal analysis, Y.L. and J.S.; Resources, L.L. and K.W.; Writing—original draft, N.W.; Writing—review & editing, Z.Y. and J.Z.; Visualization, Z.D. and J.Y. (Junbo Yang); Supervision, X.S. and J.Z.; Project administration, X.S.; Funding acquisition, Z.Z. All authors have read and agreed to the published version of the manuscript.

Funding: This work is supported by the High-Level Talent Fund of Jiangsu University (JDKQ20250401), National Natural Science Foundation of China (62005107, 52405483, 62305387, 12104508), Natural Science Foundation of Jiangsu Province (BK20220519, BK20240855), China Postdoc-toral Fund (2022M721378, 2023M741417), the Natural Science Foundation of Hunan Province (Grants No. 2023JJ40683), the Foundation of NUDT (ZK23-03), the Young Elite Scientists Sponsorship Program by CAST (No. YESS20240786) and Zhenjiang key laboratory of Advanced Manufacturing of Aerospace Components (SS2023009).

Data Availability Statement: Data underlying the results presented in this paper are not publicly available at this time but may be obtained from the authors upon reasonable request.

Conflicts of Interest: The authors declare no conflicts of interest.

References

1. Piggott, A.Y.; Lu, J.; Lagoudakis, K.G.; Petykiewicz, J.; Babinec, T.M.; Vučković, J. Inverse design and demonstration of a compact and broadband on-chip wavelength demultiplexer. *Nat. Photonics* **2015**, *9*, 374–377. [CrossRef]
2. Lukin, D.M.; Dory, C.; Guidry, M.A.; Yang, K.Y.; Mishra, S.D.; Trivedi, R.; Radulaski, M.; Sun, S.; Vercruysse, D.; Ahn, G.H.; et al. 4H-silicon-carbide-on-insulator for integrated quantum and nonlinear photonics. *Nat. Photonics* **2020**, *14*, 330–334. [CrossRef]
3. Crook, A.L.; Anderson, C.P.; Miao, K.C.; Bourassa, A.; Lee, H.; Bayliss, S.L.; Bracher, D.O.; Zhang, X.; Abe, H.; Ohshima, T.; et al. Purcell enhancement of a single silicon carbide color center with coherent spin control. *Nano Lett.* **2020**, *20*, 3427–3434. [CrossRef]
4. Nagy, R.; Niethammer, M.; Widmann, M.; Chen, Y.-C.; Udvarhelyi, P.; Bonato, C.; Hassan, J.U.; Karhu, R.; Ivanov, I.G.; Son, N.T.; et al. High-fidelity spin and optical control of single silicon-vacancy centres in silicon carbide. *Nat. Commun.* **2019**, *10*, 1954. [CrossRef]
5. Liu, T.; Qin, M.; Wu, F.; Xiao, S. High-efficiency optical frequency mixing in an all-dielectric metasurface enabled by multiple bound states in the continuum. *Phys. Rev. B* **2023**, *107*, 075441. [CrossRef]
6. Ou, H.; Shi, X.; Lu, Y.; Kollmuss, M.; Steiner, J.; Tabouret, V.; Syväjärvi, M.; Wellmann, P.; Chaussende, D. Novel photonic applications of silicon carbide. *Materials* **2023**, *16*, 1014. [CrossRef] [PubMed]
7. Jiang, H.; Sun, K.; Jia, Y.; Cai, Y.; Uriel, L.; Han, Z. Tunable Second Harmonic Generation with Large Enhancement in A Nonlocal All-Dielectric Metasurface over A Broad Spectral Range. *Adv. Opt. Mater.* **2024**, *12*, 202303229. [CrossRef]
8. Yang, C.; Cai, S.; Li, J.; Gong, H.; Liu, Z.; Chen, J.; Fu, G.; Liu, X.; Pan, P.; Liu, G. High Q transparency, strong third harmonic generation, and giant nonlinear chirality driven by toroidal dipole-quasi-BIC. *Appl. Phys. Lett.* **2024**, *125*, 181702. [CrossRef]
9. Cai, S.; Zhong, S.; Liu, X.; Liu, G.; Chen, J.; Liu, Z. Efficiently spatial field localization enabled second-harmonic and sum-frequency generation in an etchless $LiNbO_3$ layer by guided resonant quasi-bound states in the continuum. *Appl. Phys. Lett.* **2023**, *123*, 111701. [CrossRef]
10. Li, X.; Ma, J.; Liu, S.; Huang, P.; Chen, B.; Wei, D.; Liu, J. Efficient second harmonic generation by harnessing bound states in the continuum in semi-nonlinear etchless lithium niobate waveguides. *Light Sci. Appl.* **2022**, *11*, 317. [CrossRef]
11. Shi, X.; Fan, W.; Hansen, A.K.; Chi, M.; Yi, A.; Ou, X.; Rottwitt, K.; Ou, H. Thermal Behaviors and Optical Parametric Oscillation in 4H-Silicon Carbide Integrated Platforms. *Adv. Photonics Res.* **2021**, *2*, 2100068. [CrossRef]
12. Shi, X.; Lu, Y.; Peng, N.; Rottwitt, K.; Ou, H. High-performance polarization-independent beam splitters and MZI in silicon carbide integrated platforms for single-photon manipulation. *J. Light. Technol.* **2022**, *40*, 7626–7633. [CrossRef]
13. Li, J.; Wang, R.; Afridi, A.A.; Lu, Y.; Shi, X.; Sun, W.; Ou, H.; Li, Q. Efficient Raman lasing and Raman–Kerr interaction in an integrated silicon carbide platform. *ACS Photonics* **2024**, *11*, 795–800. [CrossRef] [PubMed]
14. Afridi, A.A.; Lu, Y.; Shi, X.; Wang, R.; Li, J.; Li, Q.; Ou, H. 4H–SiC microring resonators—Opportunities for nonlinear integrated optics. *Appl. Phys. Lett.* **2024**, *124*, 170502. [CrossRef]
15. Shi, X.; Zhang, J.; Fan, W.; Lu, Y.; Peng, N.; Rottwitt, K.; Ou, H. Compact low-birefringence polarization beam splitter using vertical-dual-slot waveguides in silicon carbide integrated platforms. *Photonics Res.* **2021**, *10*, A8–A13. [CrossRef]
16. Shi, X.; Fan, W.; Lu, Y.; Hansen, A.K.; Chi, M.; Yi, A.; Ou, X.; Rottwitt, K.; Ou, H. Polarization and spatial mode dependent four-wave mixing in a 4H-silicon carbide microring resonator. *APL Photonics* **2021**, *6*, 076106. [CrossRef]
17. Lu, Y.; Shi, X.; Ali Afridi, A.; Wang, Y.; Tabouret, V.; Chaussende, D.; Rottwitt, K.; Ou, H. Strong third-order nonlinearity in amorphous silicon carbide waveguides. *Opt. Lett.* **2024**, *49*, 4389–4392. [CrossRef]
18. Shi, X.; Baiju, A.A.; Dhyani, V.; Wang, S.; Mohanraj, S.S.; Leong, V.; Sun, J.; Deng, B.; Zhang, J.; Wang, Y. et al. Spontaneous Parametric Down-Conversion in 4H-SiC Integrated Platform. *Laser Photonics Rev.* **2025**, *19*, 2500104. [CrossRef]
19. Simin, D.; Kraus, H.; Sperlich, A.; Ohshima, T.; Astakhov, G.; Dyakonov, V. Locking of electron spin coherence above 20 ms in natural silicon carbide. *Phys. Rev. B* **2017**, *95*, 161201. [CrossRef]
20. Zheng, Z.; Xu, L.; Huang, L.; Smirnova, D.; Hong, P.; Ying, C.; Rahmani, M. Boosting second-harmonic generation in the $LiNbO_3$ metasurface using high-Q guided resonances and bound states in the continuum. *Phys. Rev. B* **2022**, *106*, 125411. [CrossRef]
21. Radulaski, M.; Buckley, S.M.; Zhang, J.L.; Petykiewicz, J.; Mueller, K.; Lagoudakis, K.G.; Alassaad, K.; Ferro, G.; Biermann, K.; Vuckovic, J. Nanophotonics in novel $\chi^{(2)}$-materials: (111)-GaAs and 3C-SiC. *Nonlinear Opt.* **2015**, *NM3B*, 3.
22. Shi, X.; Lu, Y.; Wang, S.; Dhyani, V. Type-II Second-Order Nonlinear Processes in Silicon Carbide Nanophotonic Waveguides. In *CLEO: Science and Innovations*; Optica Publishing Group: Washington, DC, USA, 2024; pp. 1–2 .
23. Carletti, L.; Li, C.; Sautter, J.; Staude, I.; De Angelis, C.; Li, T.; Neshev, D.N. Second harmonic generation in monolithic lithium niobate metasurfaces. *Opt. Express* **2019**, *27*, 33391–33398. [CrossRef] [PubMed]
24. Chen, Y.-C.; Salter, P.S.; Niethammer, M.; Widmann, M.; Kaiser, F.; Nagy, R.; Morioka, N.; Babin, C.; Erlekampf, J.; Berwian, P.; et al. Laser writing of scalable single color centers in silicon carbide. *Nano Lett.* **2019**, *19*, 2377–2383. [CrossRef]
25. Wang, J.; Zhou, Y.; Zhang, X.; Liu, F.; Li, Y.; Li, K.; Liu, Z.; Wang, G.; Gao, W. Efficient generation of an array of single silicon-vacancy defects in silicon carbide. *Phys. Rev. Appl.* **2017**, *7*, 064021. [CrossRef]
26. Xin, C.J.; Mishra, J.; Chen, C.; Zhu, D.; Shams-Ansari, A.; Langrock, C.; Sinclair, N.; Wong, F.N.; Fejer, M.M.; Lonृcar, M. Spectrally separable photon-pair generation in dispersion engineered thin-film lithium niobate. *Opt. Lett.* **2022**, *47*, 2830–2833. [CrossRef]

27. Hsu, C.W.; Zhen, B.; Stone, A.D.; Joannopoulos, J.D.; Soljačić, M. Bound states in the continuum. *Nat. Rev. Mater.* **2016**, *1*, 16048. [CrossRef]
28. Yan, M.; Sun, K.; Ning, T.Y.; Zhao, L.N.; Ren, Y.Y.; Huo, Y.Y. Numerical study of the low-threshold nanolaser based on quasi-bound states in the continuum supported by resonant waveguide grating structures. *Acta Phys. Sin.* **2023**, *72*, 044202. [CrossRef]
29. Widmann, M.; Lee, S.-Y.; Rendler, T.; Son, N.T.; Fedder, H.; Paik, S.; Yang, L.-P.; Zhao, N.; Yang, S.; Booker, I.; et al. Coherent control of single spins in silicon carbide at room temperature. *Nat. Mater.* **2015**, *14*, 164–168.
30. Takemoto, K.; Nambu, Y.; Miyazawa, T.; Sakuma, Y.; Yamamoto, T.; Yorozu, S.; Arakawa, Y. Quantum key distribution over 120 km using ultrahigh purity single-photon source and superconducting single-photon detectors. *Sci. Rep.* **2015**, *5*, 14383. [CrossRef]
31. Kuo, P.S.; Bravo-Abad, J.; Solomon, G.S. Second-harmonic generation using quasi-phasematching in a GaAs whispering-gallery-mode microcavity. *Nat. Commun.* **2014**, *5*, 3109. [CrossRef]
32. Anouar, R.; Wang, R.; Li, J.; Tang, X.; Thomas, G.; Oliver, S.; Li, Q.; Ma, L. Entangled photon pair generation in an integrated SiC platform. *Light Sci. Appl.* **2024** , *13*, 110.
33. Brugnolo, P.; Arslanagi'c, S.; Jacobsen, R.E. Bound states in the continuum in cylindrical all-dielectric metasurface cavities. *Phys. Rev. Lett.* **2025**, *134*, 096902. [CrossRef]
34. Abujetas, D.R.; S'anchez-Gil, J.A. Near-field excitation of bound states in the continuum in all-dielectric metasurfaces through a coupled electric/magnetic dipole model. *Nanomaterials* **2021**, *11*, 998. [CrossRef]
35. Holloway, C.L.; Love, D.C.; Kuester, E.F.; Gordon, J.A.; Hill, D.A. Use of generalized sheet transition conditions to model guided waves on metasurfaces/metafilms. *IEEE Trans. Antennas Propag.* **2012**, *60*, 5173–5186. [CrossRef]
36. Abujetas, D.R.; Sanchez-Gil, J.A.; S'aenz, J.J. Generalized Brewster effect in high-refractive-index nanorod-based metasurfaces. *Opt. Express* **2018**, *26*, 31523–31541. [CrossRef]
37. Ahler, L.C.; Ulsig, E.Z.; Stanton, E.J.; Godoy, P.H.; Weight, S.C.; Nader, N.; Leger, A.Z.; Degli-Eredi, I.; Mirin, R.P.; Volet, N. Second-order nonlinear frequency conversion in InGaP-on-insulator waveguides. *Opt. Lett.* **2025**, *50*, 3652–3655. [CrossRef]
38. Zhou, J.; Li, T.; Zhao, X.; Xu, R.; Zhang, X.; Chang, C.; Cerqueira, G.; Fu, K.; Xu, M.; He, Z.; et al. The second-order nonlinear optical properties of κ-phase gallium oxide. *APL Mater.* **2025**, *13*, 101106. [CrossRef]
39. Liu, T.; Qin, M.; Tu, X.; Liu, Y.; Wu, F.; Xiao, S. Second-harmonic and sum-frequency generation from dielectric metasurfaces empowered by multiple quasibound states in the continuum. *Appl. Phys.* **2025**, *58*, 055104. [CrossRef]
40. Liu, S.; Sinclair, M.B.; Saravi, S.; Keeler, G.A.; Yang, Y.; Reno, J.; Peake, G.M.; Setzpfandt, F.; Staude, I.; Pertsch, T.; et al. Resonantly Enhanced Second-Harmonic Generation Using III-V Semiconductor All-Dielectric Metasurfaces *NanoLett* **2016**, *16*, 5426–5432. [CrossRef]
41. Wang, Z.; Li, B.; Lu, N.; Han, Z.; Xu, L.; Rahmani, M.; Jia, Y.; Chen, F. Highly efficient ultraviolet harmonic generation based on coupled guided mode resonances in lithium niobate metasurfaces. *Laser Photonics Rev.* **2025**, *19*, e01010. [CrossRef]
42. Gao, S.; Wang, Z.; Lu, N.; Xu, L.; Han, Z.; Rahmani, M.; Jia, Y.; Chen, F. Lithium tantalate resonant metasurfaces for highly efficient ultraviolet harmonic generation. *Appl. Phys. Rev.* **2025**, *12*, 031404. [CrossRef]
43. Vincent, P.; Hoon, H.; Eric, C.; Sun, Z. Hybrid integration of 2D materials for on-chip nonlinear photonics. *Light Adv. Manuf.* **2023**, *4*, 311–333.

https://doi.org/10.3390/photonics13040311